Bounding dark charges on binary black holes using gravitational waves

Pawan Kumar Gupta,[1,2] Thomas F. M. Spieksma,[2] Peter T. H. Pang,[1,2]
Gideon Koekoek,[1,3] and Chris Van Den Broeck[1,2]

[1]*Nikhef—National Institute for Subatomic Physics, Science Park 105, 1098 XG Amsterdam, Netherlands*
[2]*Institute for Gravitational and Subatomic Physics (GRASP), Utrecht University, Princetonplein 1, 3584 CC Utrecht, Netherlands*
[3]*Department of Gravitational Waves and Fundamental Physics, Maastricht University, P.O. Box 616, 6200 MD Maastricht, Netherlands*

(Received 25 July 2021; accepted 6 August 2021; published 22 September 2021)

In models of minicharged dark matter associated with a hidden $U(1)$ symmetry, astrophysical black holes may acquire a "dark" charge, in such a way that the inspiral dynamics of binary black holes can be formally described by an Einstein-Maxwell theory. Charges enter the gravitational wave signal predominantly through a dipole term, but their effect is known to effectively first post-Newtonian order in the phase, which enables measuring the size of the charge-to-mass ratios $|q_i/m_i|$, $i = 1, 2$, of the individual black holes in a binary. We set up a Bayesian analysis to discover, or constrain, dark charges on binary black holes. After testing our framework in simulations, we apply it to selected binary black hole signals from the second gravitational wave transient catalog, namely, those with low masses so that most of the signal-to-noise ratio is in the inspiral regime. We find no evidence for charges on the black holes and place typical 1σ bounds on the charge-to-mass ratios of $|q_i/m_i| \lesssim 0.2$–0.3.

DOI: 10.1103/PhysRevD.104.063041

I. INTRODUCTION

The Advanced LIGO [1] and Advanced Virgo [2] gravitational wave (GW) detectors have so far found more than 50 candidate signals [3], the majority being from coalescing binary black holes [4–8], in addition to two binary neutron star inspirals [9,10] and two neutron star–black hole events [11]. In the analyses of the binary black hole signals, the sources were assumed to be well modeled as pure vacuum spacetime, although tests of general relativity were performed which allowed for deviations from the dynamics predicted by Einstein's theory [12–16]. In this work, we will look into another possible source for modifications in binary black hole dynamics, namely, electric charge.

As is well known, astrophysical black holes are unlikely to be able to accrue large amounts of electric charge, at least in the context of the Standard Model of particle physics (see, e.g., [17] for an overview). Kinematic buildup of charge through infall of electrons is limited by the ratio of electron mass m_e to charge e, to[1] $Q/M \leq m_e/e \simeq 5 \times 10^{-22}$, with Q and M, respectively, the charge and mass of the black hole. Also, dynamical processes such as charge accretion by a rotating black hole in a magnetic field B can produce charge-to-mass ratios of only $Q/M \lesssim 1.7 \times 10^{-20}(M/M_\odot)(B/\mathrm{G})$ [18]. Moreover, surrounding plasma in the form of interstellar matter will discharge even an extremal black hole with $Q = M$ on a timescale of $\tau \sim 10^{-6}$ s [19].

The situation is different if one considers so-called minicharged dark matter models [20,21], which involve new fermions that are charged under a hidden $U(1)$ symmetry and whose "dark" charges are much smaller than that of the electron. Such minicharged particles are viable cold dark matter candidates and have been searched for in a variety of observations and experiments [22–34]. For a dark fermion with mass m and charge q, it is possible to have $m/q > 1$, in which case values of $Q/M \simeq 1$ can be attained, and discharge timescales by the surrounding (dark matter) plasma can be on the order of billions of years [17].

Assuming a single dark fermion and dark photon, the interaction of the hidden sector with gravity can be described by an Einstein-Maxwell action:

$$S = \int d^4x\sqrt{-g}\left[\frac{R}{16\pi} - \frac{1}{4}F_{\mu\nu}F^{\mu\nu} + 4\pi A_\mu j^\mu\right], \quad (1)$$

with g the determinant of the metric $g_{\mu\nu}$, A_μ the vector potential of the hidden $U(1)$ interaction, $F_{\mu\nu} = \nabla_\mu A_\nu - \nabla_\nu A_\mu$ the associated field tensor, and j^μ the hidden current. Here, we want to look at the inspiral of binary black holes in the presence of a dark sector and search for, or put

[1]In this paper, we use units such that $G = c = 4\pi\epsilon_0 = 1$, with ϵ_0 the electric permittivity of the vacuum.

bounds on, dark charges which may be carried by them, using some of the GW signals that have been detected. The leading post-Newtonian modification to the phase is at −1PN in the usual notation, corresponding to dipole radiation. This is mostly determined by the combination

$$\xi = \left| \frac{q_1}{m_1} - \frac{q_2}{m_2} \right|, \tag{2}$$

where (q_1, q_2) and (m_1, m_2) are, respectively, the charges and masses of the individual black holes [17,35]. However, Khalil *et al.* [36] also computed higher-order effects, at 0PN and 1PN orders in phase, in the context of Einstein-Maxwell-dilaton theory, which reduces to Einstein-Maxwell theory when scalar charges are set to zero. Since these beyond-leading-order contributions also depend on different combinations of q_1/m_1 and q_2/m_2 from the one in Eq. (2), including them will allow us to make statements on these two quantities separately. Thus, our gravitational waveform model will include these modifications to the point particle inspiral phase, in addition to effects of (precessing) spins, which start from 1.5PN order. Finally, though leading-order modifications of the ringdown spectrum of the remnant black hole resulting from the merger have been computed [37–41], here we will focus only on the post-Newtonian inspiral, since to our knowledge the behavior at plunge and merger, which connects the early inspiral to the ringdown, has yet to be analytically investigated in the presence of charge. We will be particularly interested in relatively low-mass binary black hole signals, for which inspiral dominates the signal-to-noise ratio.

This paper is structured as follows. In Sec. II, we explain our waveform approximant and the data analysis setup. In Sec. III, we describe simulations that were done to provide a basic validation of the analysis framework. Section IV applies our methodology to a selection of detected signals. A summary and conclusions are provided in Sec. V.

II. WAVEFORM MODEL AND ANALYSIS FRAMEWORK

Our baseline waveform model will be the frequency domain inspiral-merger-ringdown approximant IMRPhenomPv2 [42–44], which we modify to reflect the presence of charges. This waveform stitches together in C^1 fashion (a) an *inspiral* regime which mostly follows the post-Newtonian description; (b) a phenomenological *intermediate* regime describing the late inspiral and plunge; and (c) a phenomenological *merger-ringdown* regime. Spin precession is captured by "twisting up" an underlying aligned-spin model [45,46]. Since with current detectors most of our information tends to come from the phase rather than the amplitude (though also see [47,48]), we will focus on the former and, in particular, on the inspiral phase. When electric charges are small and the inspiral is mainly driven by the tensor quadrupole flux, a good approximation to the inspiral phase is given by

$$\phi_{\rm Ins}(v) = 2\pi f t_c - \varphi_c - \pi/4 + \frac{1}{v^5}\left[\frac{\rho^{\rm QD}_{-2}}{v^2} + \rho^{\rm QD}_0 + \rho^{\rm QD}_2 v^2 + \phi^{\text{higher-order}}_{\rm Ins}(v)\right]. \tag{3}$$

Here, t_c and φ_c are, respectively, a reference time and reference phase. One has $v = (\pi M f)^{1/3}$, with f the GW frequency and where M is a "dressed" total mass; specifically, $M = G_{12}\bar{M}$, with $G_{12} = 1 - q_1 q_2/(m_1 m_2)$, where $\bar{M}$ is the observed total mass in the absence of charges. The first three terms in the square brackets include the charge-induced modifications to the phase computed by Khalil *et al.* [36] up to 1PN order. The leading-order (−1PN) contribution is set by

$$\rho^{\rm QD}_{-2} = -\frac{5 G_{12}}{3584\nu}\left(\frac{q_1}{m_1} - \frac{q_2}{m_2}\right)^2, \tag{4}$$

with $\nu = m_1 m_2/M^2$ the symmetric mass ratio. The expressions for $\rho^{\rm QD}_0$ and $\rho^{\rm QD}_2$ will not be shown explicitly here, since they are obtained straightforwardly from the ones in Ref. [36] [see their Eqs. (3.34a)–(3.34c) and Appendix B] by setting scalar charges to zero but retaining electric charges. These coefficients further reduce to the usual 0PN and 1PN coefficients for the vacuum case when electric charges are also set to zero. Finally, $\phi^{\text{higher-order}}_{\rm Ins}$ collects all higher-order contributions in v, including PN contributions as well as phenomenological corrections to the late inspiral, as detailed in Ref. [44].

In the IMRPhenomPv2 approximant, the inspiral regime is stitched onto the intermediate regime at a frequency f such that $Mf = 0.018$. Since we do not know how charges affect the latter regime, one option would be to smoothly let the waveform go to zero around that frequency, e.g., by applying a Planck tapering window [49]. However, especially when performing parameter estimation on high-mass systems for which the merger is well inside the detectors' sensitive band, we found a tendency for the tapered template waveform to try and match part of the post-inspiral signal, leading to a significant underestimation of the masses. As a pragmatic solution, we opt to not taper the waveform; instead, we will analyze only signals for which less than 5% of the matched-filtering signal-to-noise ratio is contained in the regime $Mf > 0.018$. Note that this transition always precedes the nominal last stable orbit [given by $Mf_{\rm LSO} = 1/(6^{3/2}\pi) \simeq 0.022$], so that in this way we select signals for which only the inspiral has significant power in the band.

Next, we turn to our data analysis framework. Given a detected binary black hole coalescence signal, a waveform approximant $\tilde{h}_{\rm C}(f)$ with modified phasing as in Eq. (3) can be viewed as corresponding to a Bayesian hypothesis $\mathcal{H}_{\rm C}$, which states that one or both of the black holes carried a Maxwell charge. If, on the other hand, charges are

restricted to zero, the associated waveform model $\tilde{h}_{\rm NC}$ defines a hypothesis $\mathcal{H}_{\rm NC}$, stating that no charges were present. Given a hypothesis $\mathcal{H}$, data d, and whatever background information $\mathcal{I}$ we may possess, a Bayesian evidence is obtained through [50]

$$p(d|\mathcal{H},\mathcal{I}) = \int d\bar{\theta} p(d|\mathcal{H},\bar{\theta},\mathcal{I}) p(\bar{\theta}|\mathcal{H},\mathcal{I}). \tag{5}$$

The integral is over the parameters $\bar{\theta}$ (masses, spins, possibly electric charges, etc.) that enter the waveform model $\tilde{h}(\bar{\theta};f)$ associated with $\mathcal{H}$. $p(\bar{\theta}|\mathcal{H},\mathcal{I})$ is the prior density, and the likelihood $p(d|\mathcal{H},\bar{\theta},\mathcal{I})$ is given by

$$p(d|\mathcal{H},\bar{\theta},\mathcal{I}) \propto \exp\left[-\langle d-h(\bar{\theta})|d-h(\bar{\theta})\rangle/2\right]. \tag{6}$$

The noise-weighted inner product $\langle\cdot|\cdot\rangle$ is defined as

$$\langle a|b\rangle = 4\mathrm{Re}\int_{f_{\rm low}}^{f_{\rm high}} df \frac{\tilde{a}^*(f)\tilde{b}(f)}{S_n(f)}, \tag{7}$$

where $f_{\rm low}$ and $f_{\rm high}$ are, respectively, the detector's lower cutoff frequency and the frequency at which a given signal ends and S_n is the (one-sided) power spectral density of the noise. In this paper, we will set $f_{\rm low} = 20$ Hz, and $f_{\rm high}$ is determined by the parameters entering the IMRPhenomPv2 waveform. Given our hypotheses $\mathcal{H}_{\rm C}$ and $\mathcal{H}_{\rm NC}$, the general expression for the evidence (5) enables computation of a Bayes factor which can be used to rank the hypotheses:

$$B^{\rm C}_{\rm NC} \equiv \frac{p(d|\mathcal{H}_{\rm C},\mathcal{I})}{p(d|\mathcal{H}_{\rm NC},\mathcal{I})}. \tag{8}$$

Apart from hypothesis ranking, the Bayesian framework also allows us to perform parameter estimation; in particular, the posterior density function (PDF) for the parameters $\bar{\theta}$ follows from Bayes' theorem:

$$p(\bar{\theta}|\mathcal{H},d,\mathcal{I}) = \frac{p(d|\mathcal{H},\bar{\theta},\mathcal{I})p(\bar{\theta}|\mathcal{H},\mathcal{I})}{p(d|\mathcal{H},\mathcal{I})}. \tag{9}$$

The one-dimensional PDF $p(\lambda|\mathcal{H},d,\mathcal{I})$ for a particular parameter λ is obtained from this by integrating out all other parameters.

In our studies, the likelihood function of Eq. (6) is sampled using the lalinference_nest algorithm in the LALInference library [51], while the waveform model described in the previous section was implemented as an extension of the IMRPhenomPv2 approximant in the LALSimulation library of LALSuite [52].

Together with spin-related parameters, the intrinsic parameters being sampled over directly are the (dressed) total mass M, the mass ratio $q = m_2/m_1$ (with the convention $m_2 \le m_1$), and the charge-to-mass ratios $\sigma_1 \equiv q_1/m_1$ and $\sigma_2 \equiv q_2/m_2$. For M and q, we use uniform priors chosen wide enough so as to accommodate the supports of the PDFs (with an upper bound of 1 for q). Regarding the σ_i, for the examples in this paper, a uniform prior spanning $\sigma_i \in [-2,2]$ amply sufficed; here, the sampling was done with the additional constraint $\sigma_1\sigma_2 < 1$, corresponding to the requirement of inspiraling orbits. Priors on the spin magnitudes a_1 and a_2 are taken to be uniform in the range [0, 0.99], and priors on spin directions are uniform on the sphere. Both for simulated signals and for template waveforms we impose the Kerr-Newman condition for the presence of black hole horizons, i.e., $a_i^2 + \sigma_i^2 \le 1$, $i = 1, 2$ [53]. For the extrinsic parameters, the priors on sky position and the orientation of the orbital plane at some reference frequency are also uniform on the sphere. We use a uniform-in-volume prior on distance, up to a maximum distance needed to accommodate the PDF.

III. SIMULATIONS

We now turn to the simulations we performed to gain insight into the measurability of black hole charges for signals typical of the long-duration binary black hole signals seen in the second gravitational wave transient catalog (GWTC-2) [8]. Signals were injected into a network consisting of the two Advanced LIGO interferometers and Advanced Virgo, assuming stationary, Gaussian noise following the projected design sensitivities of these observatories [1,2]. As explained in Sec. II, we will focus on signals that are relatively low mass, such that no more than 5% of signal-to-noise ratio (SNR) is present beyond $Mf = 0.018$; we require this of our injections as well. Also, we pick injected chirp masses $\mathcal{M} = M\nu^{3/5}$ in the range $[7,9]M_\odot$ and mass ratios $q \in [0.4,1]$, choices that are representative of those signals in GWTC-2 that satisfy

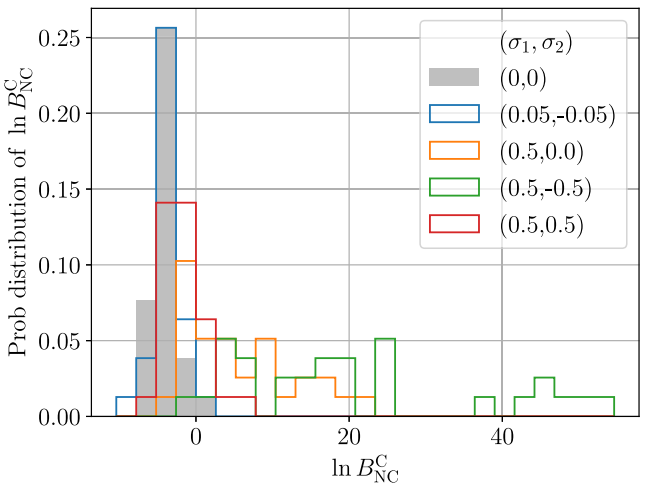

FIG. 1. Histograms for $\ln B^{\rm C}_{\rm NC}$ for 67 choices of masses and spins with ranges as detailed in the main text and the five different choices of (σ_1,σ_2) indicated in the legend.

TABLE I. Values of $\ln B^{\mathrm{C}}_{\mathrm{NC}}$ for different injected values of (σ_1, σ_2), in the case of an injection with $(m_1, m_2) = (13.87, 6.36)M_\odot$ and an SNR of 12.52, for which PDFs are shown in Figs. 2–6.

(σ_1, σ_2)	(0, 0)	(0.05, −0.05)	(0.5, 0)	(0.5, −0.5)	(0.5, 0.5)
$\ln B^{\mathrm{C}}_{\mathrm{NC}}$	−4.19	−3.11	10.25	43.82	−1.01

our post-inspiral SNR requirement. For the purpose of studying the behavior of $\ln B^{\mathrm{C}}_{\mathrm{NC}}$, SNRs are chosen to be in the range 10–15, again representative of the signals in GWTC-2 that we will analyze later on. For (σ_1, σ_2), we pick the following values:

(i) $(\sigma_1, \sigma_2) = (0, 0)$,
(ii) $(\sigma_1, \sigma_2) = (0.05, -0.05)$,
(iii) $(\sigma_1, \sigma_2) = (0.5, 0)$,
(iv) $(\sigma_1, \sigma_2) = (0.5, -0.5)$, and
(v) $(\sigma_1, \sigma_2) = (0.5, 0.5)$,

where the larger numbers are inspired by Fisher matrix estimates on the measurability with Advanced LIGO and Virgo of the strength of a dipole contribution to the phase [17,35].

First we look at $\ln B^{\mathrm{C}}_{\mathrm{NC}}$ for 67 injections in stationary, Gaussian noise for an Advanced LIGO-Virgo network, with (dressed) masses and spins in the ranges specified above, SNRs in the range 10–15, and our five different choices for (σ_1, σ_2). Histograms for the log Bayes factor are given in Fig. 1. The following trends are seen.

(i) For $(\sigma_1, \sigma_2) = (0, 0)$, all of the $\ln B^{\mathrm{C}}_{\mathrm{NC}}$ are negative except for one at $\ln B^{\mathrm{C}}_{\mathrm{NC}} = 0.50$, consistent with the absence of charges in the injected signals.
(ii) Also, for $(\sigma_1, \sigma_2) = (0.05, -0.05)$, the great majority of $\ln B^{\mathrm{C}}_{\mathrm{NC}}$ are negative, indicating that charge-to-mass ratios of this size are not discernable at the given SNRs.
(iii) For $(\sigma_1, \sigma_2) = (0.5, 0)$, most signals show a positive $\ln B^{\mathrm{C}}_{\mathrm{NC}}$.
(iv) The choice $(\sigma_1, \sigma_2) = (0.5, -0.5)$ leads to the highest log Bayes factors, consistent with the fact that this yields the strongest leading-order (−1PN) contribution to the phasing; see Eqs. (3) and (4).
(v) However, for $(\sigma_1, \sigma_2) = (0.5, 0.5)$, though the individual charge-to-mass ratios are large, the −1PN contribution vanishes identically, leading to small (in fact, mostly negative) values of $\ln B^{\mathrm{C}}_{\mathrm{NC}}$.

Next, we turn to parameter estimation. As a representative example, we focus on an injected signal with $(m_1, m_2) = (13.87, 6.36)M_\odot$ and an SNR of 12.52. Bearing in mind the invariance of our waveform model under $(\sigma_1, \sigma_2) \to (-\sigma_1, -\sigma_2)$, we find it convenient to show posteriors for $|\sigma_1|$, $|\sigma_2|$, and $\xi = |\sigma_1 - \sigma_2|$. Log Bayes factors for the different injected (σ_1, σ_2) are shown in Table I; they are consistent with the trends observed in Fig. 1.

Figure 2 shows the results for the above mass pair and $(\sigma_1, \sigma_2) = (0, 0)$. We see that the posterior densities for the $|\sigma_i|$ are consistent with zero charges. They do show a peak away from zero; this is because random noise fluctuations cause the peaks of the distributions for the σ_i themselves (before taking the absolute value) to be away from zero. Bounds of $|\sigma_i| \lesssim 0.26$ are obtained at

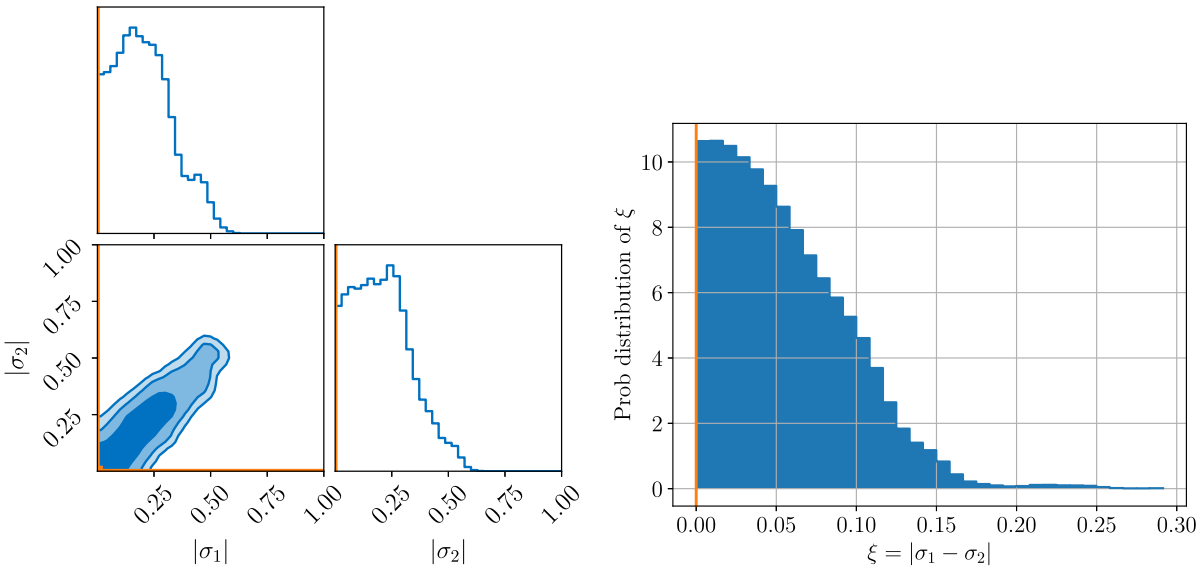

FIG. 2. Posterior distributions for an injection with $(m_1, m_2) = (13.87, 6.36)M_\odot$ at an SNR of 12.52 and $(\sigma_1, \sigma_2) = (0, 0)$. The left panel shows a corner plot for the posterior distributions of $|\sigma_1|$ and $|\sigma_2|$ (with the contours enclosing, respectively, 68%, 95%, and 99.7% of probability), while the right one is the posterior for $\xi = |\sigma_1 - \sigma_2|$. Here and in the analogous figures below, orange lines indicate the injected parameters.

68% confidence. A somewhat more stringent bound is obtained for ξ, namely, $\xi \lesssim 0.07$ at the same confidence level; this is again as expected, because it sets the leading-order term in the phase.

Next, Fig. 3 shows results for the same mass pair, but now $(\sigma_1, \sigma_2) = (0.05, -0.05)$. As already indicated by the log Bayes factor in Table I, such values of σ_i are not detectable, and indeed the posteriors are consistent with zero charges. However, we note that the posterior for ξ does show a slight peak near $|\sigma_1 - \sigma_2| = 0.1$.

In Fig. 4, we consider the case $(\sigma_1, \sigma_2) = (0.5, 0)$, for which the log Bayes factor clearly indicated the presence of charge. Here, the posteriors show clear support for both $(|\sigma_1|, |\sigma_2|) = (0.5, 0)$ and $(|\sigma_1|, |\sigma_2|) = (0, 0.5)$, consistent with another symmetry of the waveform, namely, $(\sigma_1, \sigma_2) \to (\sigma_2, \sigma_1)$. Meanwhile, the posterior for ξ correctly has a strong peak near 0.5.

Figure 5 shows results for $(\sigma_1, \sigma_2) = (0.5, -0.5)$. Though the individual posteriors for the $|\sigma_i|$ are wide, there is clear support for the values $(|\sigma_1|, |\sigma_2|) = (0.5, 0.5)$. The posterior for ξ is tightly peaked near $\xi = 1$.

Finally, we consider the case $(\sigma_1, \sigma_2) = (0.5, 0.5)$, in Fig. 6. This is a case where the log Bayes factor was negative (see again Table I) presumably because of the absence of the dipole contribution together with the moderate SNR. And, indeed, the posterior for ξ is not very informative, although the ones for the $|\sigma_i|$ are consistent with the injected values.

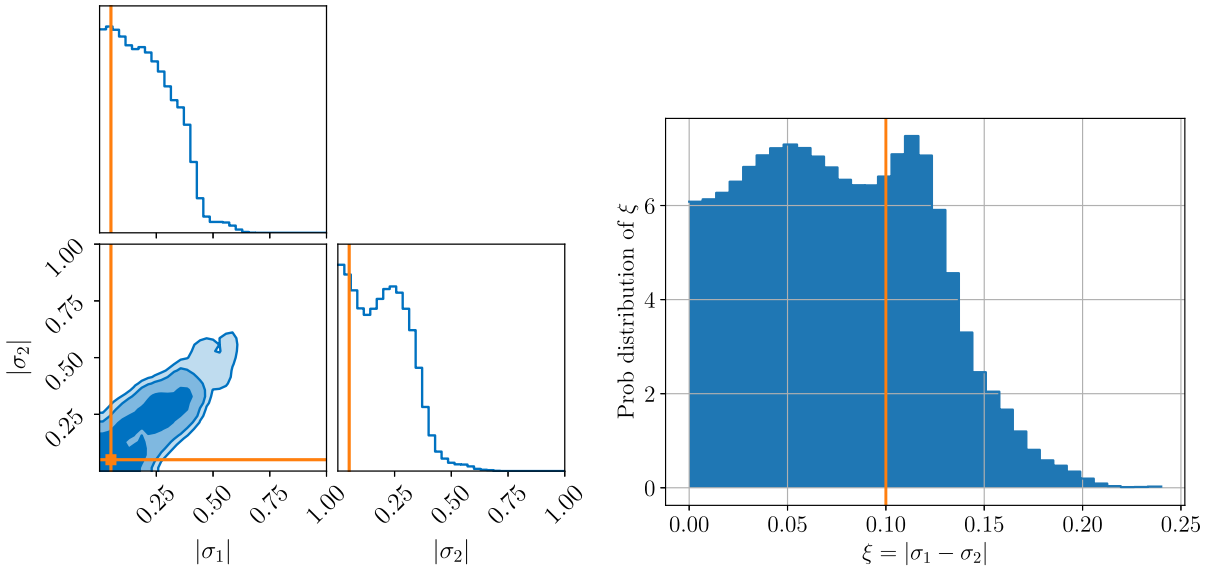

FIG. 3. The same as in Fig. 2 but for $(\sigma_1, \sigma_2) = (0.05, -0.05)$.

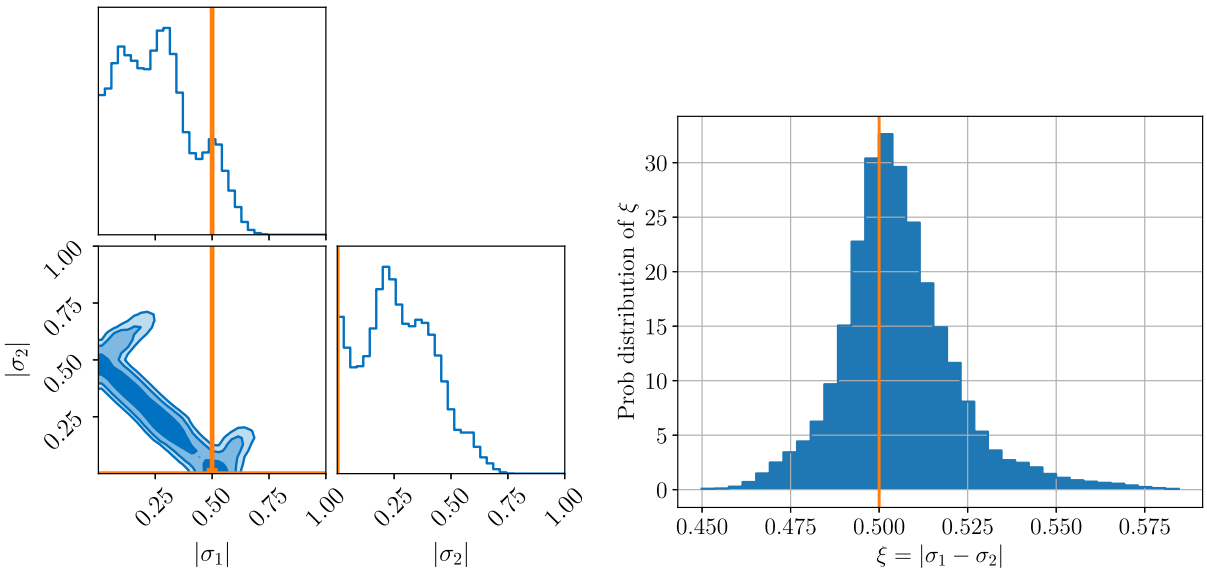

FIG. 4. The same as in Fig. 2 but for $(\sigma_1, \sigma_2) = (0.5, 0)$.

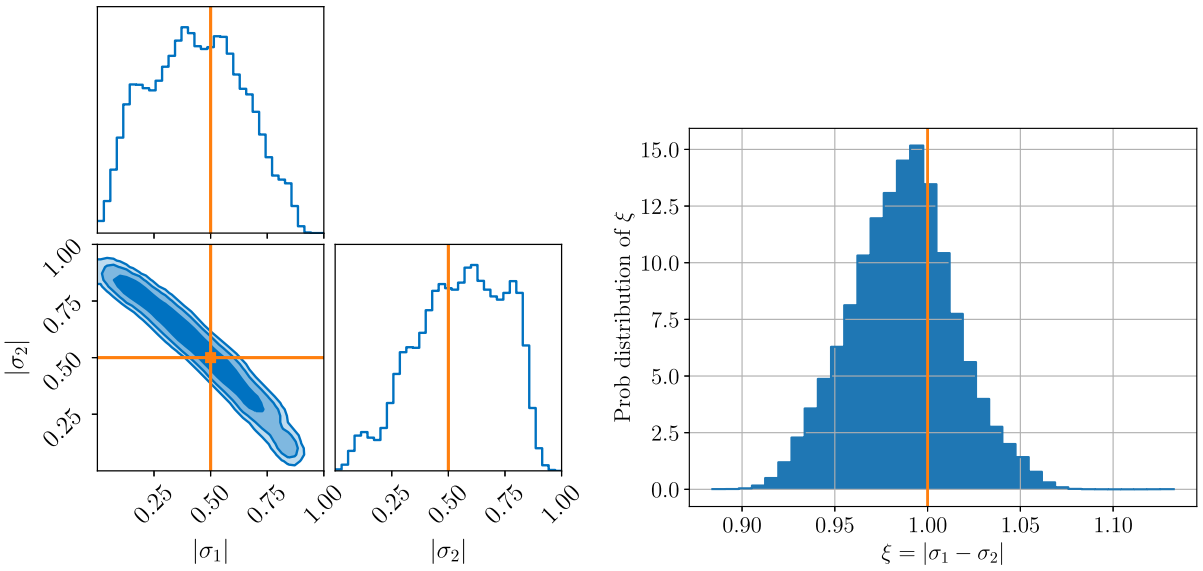

FIG. 5. The same as in Fig. 2 but for $(\sigma_1, \sigma_2) = (0.5, -0.5)$.

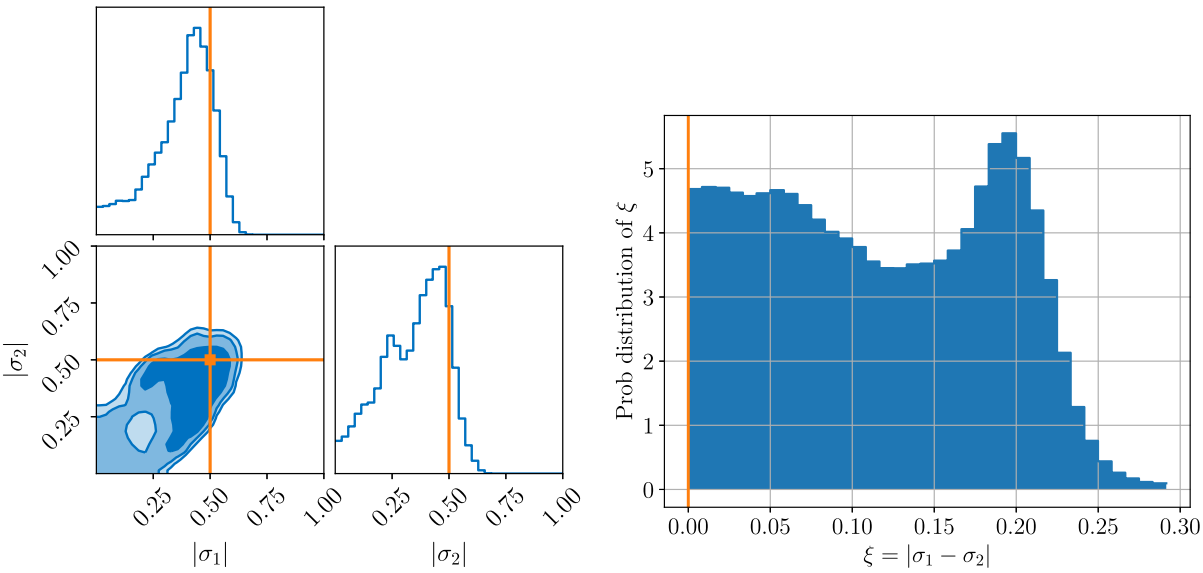

FIG. 6. The same as in Fig. 2 but for $(\sigma_1, \sigma_2) = (0.5, 0.5)$.

IV. ANALYSIS OF SELECTED BINARY BLACK HOLE SIGNALS

Let us now turn to actual signals from GWTC-2 [8] and, in particular, those that satisfy our criterion that at most 5% of the SNR resides in the post-inspiral phase, defined as $Mf > 0.018$. To assess which signals are in accordance with this benchmark, we take the median estimated parameter values reported in Refs. [7,8] and substitute them into an IMRPhenomPv2 waveform. The events we end up with are listed in Table II, which also gives the values for $\ln B^{\mathrm{C}}_{\mathrm{NC}}$. Since all log Bayes factors are negative, we find no evidence for charges in any of these.

TABLE II. The GWTC-2 events analyzed, with their log Bayes factors for charges versus no charges.

Events	GW151226	GW170608	GW190707	GW190720	GW190728	GW190924	GW190930
$\ln B^{\mathrm{C}}_{\mathrm{NC}}$	−7.52	−7.63	−2.94	−3.71	−3.11	−3.67	−3.04

For completeness, we also show posteriors for $|\sigma_1|$ and $|\sigma_2|$ (Fig. 7) and $\xi = |\sigma_1 - \sigma_2|$ (Fig. 8). Here, too, all the signals show consistency with $(\sigma_1, \sigma_2) = (0, 0)$. Events like GW190707, GW190728, and GW190924 have posteriors for the individual $|\sigma_1|$ and $|\sigma_2|$ that seem to have a peak away from zero, but, as in the case of our simulated

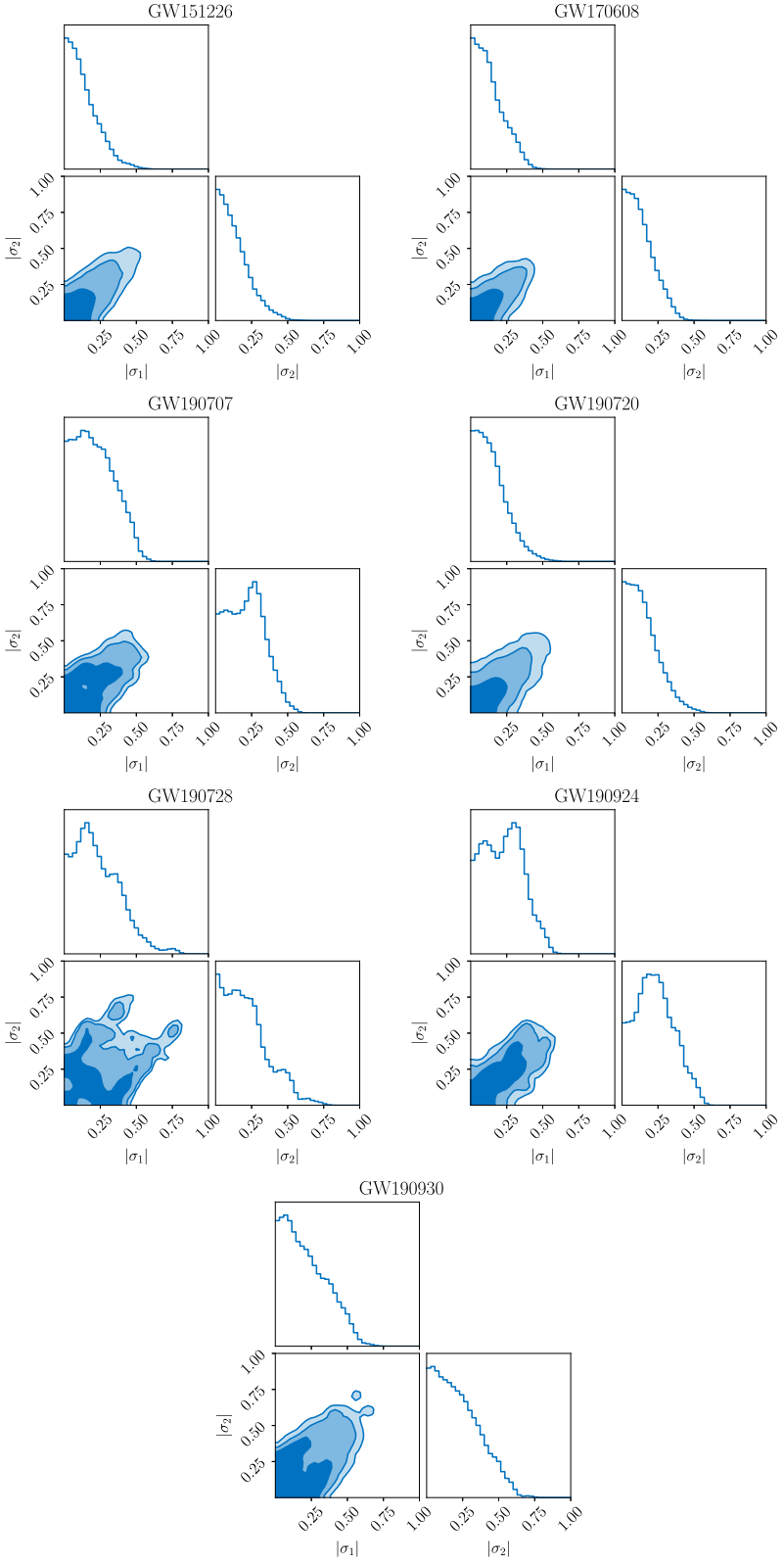

FIG. 7. Corner plots for the posteriors of $|\sigma_1|$ and $|\sigma_2|$, for the events in Table II.

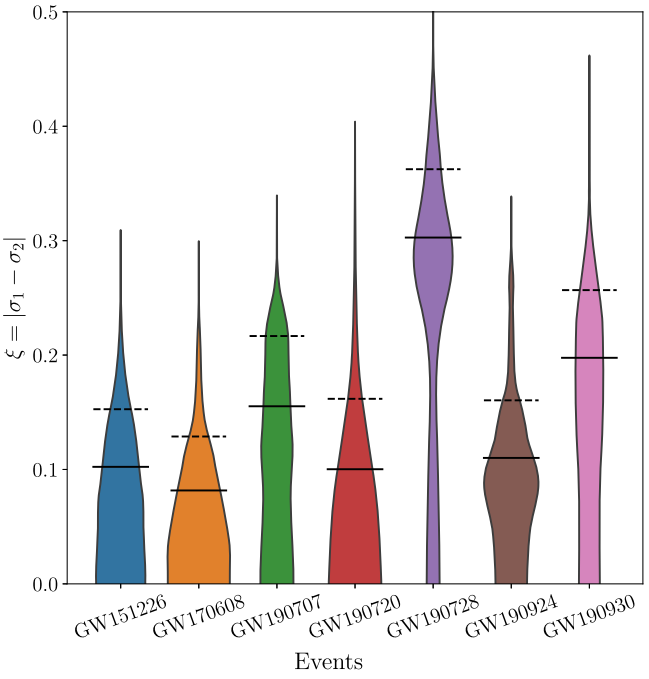

FIG. 8. Posterior densities for $\xi = |\sigma_1 - \sigma_2|$, for the events in Table II. The solid lines indicate 68% confidence levels, and the dashed lines 90% confidence levels.

signal with $(\sigma_1, \sigma_2) = (0, 0)$ (see Fig. 2), this can be attributed to noise fluctuations causing the peaks of the σ_i themselves (before taking the absolute value) to be away from zero. However, these three events also have a peak in ξ that is away from zero; in the case of GW190728, there is even a relatively strong peak at $\xi \sim 0.3$. That said, the log Bayes factor for GW190728 ($\ln B^{\mathrm{C}}_{\mathrm{NC}} = -3.11$) is below the largest log Bayes factor for injections with $(\sigma_1, \sigma_2) = (0, 0)$ shown in Fig. 1, which is $\ln B^{\mathrm{C}}_{\mathrm{NC}} = 0.50$; the same is true of all the other real events in Table II. Although the injection set in Fig. 1 pertained to stationary, Gaussian noise, we expect a more complete "background distribution" for $\ln B^{\mathrm{C}}_{\mathrm{NC}}$ in real noise to extend to even larger values. Therefore, we are not induced to conclude that charges were present on any of the binary black holes that generated the real signals we analyzed.

For all our real events, the 1σ bounds on the $|\sigma_i|$ tend to be at the level of 0.2–0.3, consistent with the zero-charge injection which we studied PDFs for in the previous section. Similarly, bounds on ξ tend to be somewhat more stringent, varying from 0.08 (for GW170608) to 0.3 (for GW190728).

V. SUMMARY AND CONCLUSIONS

We have set up a Bayesian analysis framework to search for, or constrain, (dark) electric charges on binary black holes using gravitational waves. In particular, the inspiral part of the phasing of the precessing-spin IMRPhenomPv2 inspiral-merger-ringdown waveform was modified to include the effect of such charges up to 1PN order. This was then used for both injections and template waveforms, focusing on signals with less than 5% of their SNR in the post-inspiral regime, in view of the currently unknown effect of charges during plunge and merger.

To test the analysis setup, we looked at the log Bayes factor $\ln B^{\mathrm{C}}_{\mathrm{NC}}$, comparing the hypothesis that charges are present with the one that assumes zero charges, for signals with SNRs between 10 and 15. Choosing different injected values for the charge-to-mass ratios (σ_1, σ_2), expected trends were seen in the distributions of $\ln B^{\mathrm{C}}_{\mathrm{NC}}$: (a) When the σ_i were zero or small, the great majority of our simulated signals yielded $\ln B^{\mathrm{C}}_{\mathrm{NC}} < 0$, and (b) for larger σ_i, the typical magnitude of $\ln B^{\mathrm{C}}_{\mathrm{NC}}$ was set by the strength of the leading-order contribution of charges to the phase, which is determined by $\xi = |\sigma_1 - \sigma_2|$.

As a case study for parameter estimation, we used an injection with an SNR of 12.52. PDFs were indicative of the injected (σ_1, σ_2), and, for $(\sigma_1, \sigma_2) = (0, 0)$, 1σ upper bounds came out to be $|\sigma_i| \lesssim 0.26$ and $\xi \lesssim 0.07$.

Finally, we turned to real signals from GWTC-2, again selected to have a long inspiral in band. All of the $\ln B^{\mathrm{C}}_{\mathrm{NC}}$ came out to be negative, consistent with the absence of charges, and also the PDFs for the $|\sigma_i|$ and ξ were consistent with zero charge. Typical bounds on charge-related parameters were $|\sigma_i| \lesssim 0.2$–0.3 and $\xi \lesssim 0.08$–0.3.

In this work, we focused on the inspiral regime, but charge-induced modifications of the ringdown spectrum have also been computed [37–41]. It would be of interest to search for the signature of charges in the ringdown signal of high-mass events, whose ringdown modes are starting to be probed even with Advanced LIGO and Virgo at O3 sensitivity [16]. Finally, should appropriate waveform models become available in the future, it will be interesting to see how charge measurements will sharpen when the entire inspiral-merger-ringdown process can be used.

ACKNOWLEDGMENTS

P. K. G., P. T. H. P., G. K., and C. V. D. B. are supported by the research program of the Netherlands Organisation for Scientific Research (NWO). The authors are grateful for computational resources provided by the LIGO Laboratory and supported by the National Science Foundation Grants No. PHY-0757058 and No. PHY-0823459. This research has made use of data, software, and/or Web tools obtained from the Gravitational Wave Open Science Center, a service of LIGO Laboratory, the LIGO Scientific Collaboration, and the Virgo Collaboration. LIGO is funded by the U.S. National Science Foundation. Virgo is funded by the French Centre National de Recherche Scientifique (CNRS), the Italian Istituto Nazionale della Fisica Nucleare (INFN), and the Dutch Nikhef, with contributions by Polish and Hungarian institutes.

[1] J. Aasi *et al.* (LIGO Scientific Collaboration), Classical Quant. Grav. **32**, 074001 (2015).
[2] F. Acernese *et al.* (VIRGO Collaboration), Classical Quant. Grav. **32**, 024001 (2015).
[3] https://gracedb.ligo.org/superevents/public/O3/.
[4] B. Abbott *et al.* (LIGO Scientific and Virgo Collaborations), Phys. Rev. Lett. **116**, 061102 (2016).
[5] B. P. Abbott *et al.* (LIGO Scientific and Virgo Collaborations), Phys. Rev. Lett. **116**, 241103 (2016).
[6] B. P. Abbott *et al.* (LIGO Scientific and Virgo Collaborations), Phys. Rev. X **6**, 041015 (2016); **8**, 039903(E) (2018).
[7] B. P. Abbott *et al.* (LIGO Scientific and Virgo Collaborations), Phys. Rev. X **9**, 031040 (2019).
[8] R. Abbott *et al.* (LIGO Scientific and Virgo Collaborations), Phys. Rev. X **11**, 021053 (2021).
[9] B. P. Abbott *et al.* (Virgo and LIGO Scientific Collaborations), Phys. Rev. Lett. **119**, 161101 (2017).
[10] B. P. Abbott *et al.* (LIGO Scientific and Virgo Collaborations), Astrophys. J. Lett. **892**, L3 (2020).
[11] R. Abbott *et al.* (LIGO Scientific, KAGRA, and VIRGO Collaborations), Astrophys. J. Lett. **915**, L5 (2021).
[12] B. P. Abbott *et al.* (LIGO Scientific and Virgo Collaborations), Phys. Rev. Lett. **116**, 221101 (2016); **121**, 129902(E) (2018).
[13] B. P. Abbott *et al.* (LIGO Scientific and Virgo Collaborations), Astrophys. J. Lett. **882**, L24 (2019).
[14] B. P. Abbott *et al.* (LIGO Scientific and Virgo Collaborations), Phys. Rev. Lett. **123**, 011102 (2019).
[15] B. P. Abbott *et al.* (LIGO Scientific and Virgo Collaborations), Phys. Rev. D **100**, 104036 (2019).
[16] R. Abbott *et al.* (LIGO Scientific and Virgo Collaborations), Phys. Rev. D **103**, 122002 (2021).
[17] V. Cardoso, C. F. B. Macedo, P. Pani, and V. Ferrari, J. Cosmol. Astropart. Phys. 05 (2016) 054; 04 (2020) E01.
[18] R. M. Wald, Phys. Rev. D **10**, 1680 (1974).
[19] D. M. Eardley and W. H. Press, Annu. Rev. Astron. Astrophys. **13**, 381 (1975).
[20] B. Holdom, Phys. Lett. **166B**, 196 (1986).
[21] A. De Rujula, S. L. Glashow, and U. Sarid, Nucl. Phys. **B333**, 173 (1990).
[22] K. Sigurdson, M. Doran, A. Kurylov, R. R. Caldwell, and M. Kamionkowski, Phys. Rev. D **70**, 083501 (2004); **73**, 089903(E) (2006).
[23] S. Davidson and M. E. Peskin, Phys. Rev. D **49**, 2114 (1994).
[24] S. Davidson, S. Hannestad, and G. Raffelt, J. High Energy Phys. 05 (2000) 003.
[25] S. D. McDermott, H.-B. Yu, and K. M. Zurek, Phys. Rev. D **83**, 063509 (2011).
[26] S. L. Dubovsky, D. S. Gorbunov, and G. I. Rubtsov, JETP Lett. **79**, 1 (2004).
[27] A. D. Dolgov, S. L. Dubovsky, G. I. Rubtsov, and I. I. Tkachev, Phys. Rev. D **88**, 117701 (2013).
[28] H. Gies, J. Jaeckel, and A. Ringwald, Phys. Rev. Lett. **97**, 140402 (2006).
[29] H. Gies, J. Jaeckel, and A. Ringwald, Europhys. Lett. **76**, 794 (2006).
[30] C. Burrage, J. Jaeckel, J. Redondo, and A. Ringwald, J. Cosmol. Astropart. Phys. 11 (2009) 002.
[31] M. Ahlers, Phys. Rev. D **80**, 023513 (2009).
[32] A. Haas, C. S. Hill, E. Izaguirre, and I. Yavin, Phys. Lett. B **746**, 117 (2015).
[33] A. Ball *et al.*, arXiv:1607.04669.
[34] K. Kadota, T. Sekiguchi, and H. Tashiro, arXiv:1602.04009.
[35] E. Barausse, N. Yunes, and K. Chamberlain, Phys. Rev. Lett. **116**, 241104 (2016).
[36] M. Khalil, N. Sennett, J. Steinhoff, J. Vines, and A. Buonanno, Phys. Rev. D **98**, 104010 (2018).
[37] P. Pani, E. Berti, and L. Gualtieri, Phys. Rev. Lett. **110**, 241103 (2013).
[38] P. Pani, E. Berti, and L. Gualtieri, Phys. Rev. D **88**, 064048 (2013).
[39] M. Zilhão, V. Cardoso, C. Herdeiro, L. Lehner, and U. Sperhake, Phys. Rev. D **90**, 124088 (2014).
[40] Z. Mark, H. Yang, A. Zimmerman, and Y. Chen, Phys. Rev. D **91**, 044025 (2015).
[41] O. J. C. Dias, M. Godazgar, and J. E. Santos, Phys. Rev. Lett. **114**, 151101 (2015).
[42] M. Hannam, P. Schmidt, A. Bohé, L. Haegel, S. Husa, F. Ohme, G. Pratten, and M. Pürrer, Phys. Rev. Lett. **113**, 151101 (2014).
[43] S. Husa, S. Khan, M. Hannam, M. Pürrer, F. Ohme, X. J. Forteza, and A. Bohé, Phys. Rev. D **93**, 044006 (2016).
[44] S. Khan, S. Husa, M. Hannam, F. Ohme, M. Pürrer, X. J. Forteza, and A. Bohé, Phys. Rev. D **93**, 044007 (2016).
[45] P. Schmidt, M. Hannam, and S. Husa, Phys. Rev. D **86**, 104063 (2012).
[46] P. Schmidt, F. Ohme, and M. Hannam, Phys. Rev. D **91**, 024043 (2015).
[47] R. Abbott *et al.* (LIGO Scientific and Virgo Collaborations), Phys. Rev. D **102**, 043015 (2020).
[48] R. Abbott *et al.* (LIGO Scientific and Virgo Collaborations), Astrophys. J. Lett. **896**, L44 (2020).
[49] D. J. A. McKechan, C. Robinson, and B. S. Sathyaprakash, Gravitational Waves. Proceedings of the 8th Edoardo Amaldi Conference, Amaldi 8, New York, 2009; Classical Quant. Grav. **27**, 084020 (IOP Publishing, Bristol, 2010).
[50] J. Veitch and A. Vecchio, Phys. Rev. D **81**, 062003 (2010).
[51] J. Veitch *et al.*, Phys. Rev. D **91**, 042003 (2015).
[52] LIGO Scientific Collaboration, LIGO Algorithm Library—LALSuite, free software (GPL) (2018).
[53] E. T. Newman, R. Couch, K. Chinnapared, A. Exton, A. Prakash, and R. Torrence, J. Math. Phys. (N.Y.) **6**, 918 (1965).